

Steerable *e*PCA

Zhizhen Zhao *Member, IEEE*, Lydia T. Liu, and Amit Singer

Abstract—In photon-limited imaging, the pixel intensities are affected by photon count noise. Many applications, such as 3-D reconstruction using correlation analysis in X-ray free electron laser (XFEL) single molecule imaging, require an accurate estimation of the covariance of the underlying 2-D clean images. Accurate estimation of the covariance from low-photon count images must take into account that pixel intensities are Poisson distributed, rendering the sub-optimality of the classical sample covariance estimator. Moreover, in single molecule imaging, including in-plane rotated copies of all images could further improve the accuracy of covariance estimation. In this paper we introduce an efficient and accurate algorithm for covariance matrix estimation of count noise 2-D images, including their uniform planar rotations and possibly reflection. Our procedure, *steerable ePCA*, combines in a novel way two recently introduced innovations. The first is a methodology for principal component analysis (PCA) for Poisson distributions, and more generally, exponential family distributions [1], called *ePCA*. The second is steerable PCA [2], [3], a fast and accurate procedure for including all planar rotations for PCA. The resulting principal components are invariant to the rotation and reflection of the input images. We demonstrate the efficiency and accuracy of steerable *ePCA* in numerical experiments involving simulated XFEL datasets.

Index Terms—Poisson noise, X-ray free electron laser, steerable PCA, eigenvalue shrinkage, autocorrelation analysis, image denoising.

I. INTRODUCTION

X-ray free electron laser (XFEL) is an emerging imaging technique for elucidating the three-dimensional structure of molecules [4], [5]. Single molecule XFEL imaging collects two-dimensional diffraction patterns of single particles at random orientations. The images are very noisy due to the low photon counts and the detector count-noise follows an approximately Poisson distribution. Since we only capture one diffraction pattern per particle and the particle orientations are unknown, it is challenging to reconstruct the 3-D structure at low signal-to-noise ratio (SNR). One approach is to use expectation-maximization (EM) [6], [7], which has no guarantee of the global optimality. Alternatively, assuming that the orientations are uniformly distributed over the special orthogonal group $SO(3)$, Kam’s correlation analysis [8]–[15] bypasses maximum likelihood estimation. Instead, it requires a robust estimation of the covariance matrix of the noiseless 2-D images. This serves as our main motivation for developing efficient and accurate covariance estimation and denoising methods for Poisson data.

ZZ is with the Department of Electrical and Computer Engineering, University of Illinois at Urbana-Champaign, Urbana, IL, 61820 USA e-mail: zhizhenz@illinois.edu .

LL is with the Department of Electrical Engineering and Computer Sciences, University of California at Berkeley, Berkeley, CA, 94720 e-mail: lydiatliu@berkeley.edu

AS is with the Department of Mathematics, and Program in Applied and Computational Mathematics, Princeton University, Princeton, NJ, 08544 e-mail: amits@math.princeton.edu

Principal Component Analysis (PCA) is widely used for dimension reduction and denoising of large datasets [16], [17]. However, it is most naturally designed for Gaussian data, and there is no commonly agreed upon extension to non-Gaussian settings such as exponential families [16, Sec. 14.4]. For denoising with non-Gaussian noise, popular approaches reduce it to the Gaussian case by a wavelet transform such as a Haar transform [18]; by adaptive wavelet shrinkage [18], [19]; or by approximate variance stabilization such as the Anscombe transform [20]. The latter is known to work well for Poisson signals with large parameters, due to approximate normality. However, the normal approximation breaks down for Poisson distributions with a small parameter, such as photon-limited XFEL [21, Sec. 6.6]. Other methods are based on singular value thresholding (SVT) [22], [23] and Bayesian techniques [24]. In addition, many existing methods are computationally intractable for large datasets. Recently, [1] introduced exponential family PCA (*ePCA*), which extends PCA to a wider class of distributions. It involves the eigendecomposition of a new covariance matrix estimator, constructed in a deterministic and non-iterative way using moment calculations and shrinkage. *ePCA* was shown to be more accurate than PCA and its alternatives for exponential families. Its computational cost is similar to that of PCA, it has substantial theoretical justification building on random matrix theory, and its output is interpretable.

In XFEL imaging, the orientations are uniformly distributed over $SO(3)$, and it is therefore equally likely to observe any planar rotation of the given diffraction pattern. Therefore, it makes sense to include all possible in-plane rotations of the images when performing *ePCA*. To this end, we incorporate steerable PCA, by adapting the steerable PCA algorithm [3]. We take into account the action of the group $O(2)$ on diffraction patterns by in-plane rotation and reflection. The resulting principal components are invariant to any $O(2)$ transformation of the input images. In the new algorithm, we first estimate the rotational invariant sample mean of the image dataset and use it to “prewhiten” the images (we refer to this step as prewhitening, since the mechanism is similar to that of whitening colored noise). We then compute the truncated Fourier-Bessel expansion coefficients of the prewhitened images. Since the truncated Fourier-Bessel transform is almost unitary [3], we can compute the rotational invariant sample covariance matrix in terms of the expansion coefficients. The resulting covariance matrix has block diagonal structure. For each covariance sub-block, we apply shrinkage, recoloring, and scaling as in [1] to estimate the underlying clean covariance matrix.

We illustrate the improvement in estimating the covariance matrix through image denoising. Specifically, we introduce a Wiener-type filtering of the truncated Fourier-Bessel expansion

coefficients. Rotation invariance enhances the effectiveness of e PCA in covariance estimation and thus achieves better denoising. In addition, the denoised expansion coefficients are useful in building rotationally invariant image features (i.e. bispectrum-like features [2]). We verify the benefits of steerable e PCA through numerical experiments with the simulated XFEL diffraction patterns. Similar to the case with normal PCA, the computational complexity of the steerable e PCA is lower than e PCA.

The paper is organized as follows: Section II contains the observation model (II-A) and the computation of the steerable exponential principal components (II-B). Various numerical examples comparing the steerable e PCA and e PCA are presented in Section III. An implementation of steerable e PCA in MATLAB is publicly available at github.com/zhizhenz/sepcal/.

II. METHODS

A. The observation model

We adopt the same observation model as in [1]. The observed noisy images $Y \in \mathbb{R}^p$ (i.e., p is the number of pixels) are random vectors with some unknown distribution and follow a hierarchical model. First, a latent vector—or hyperparameter— $\theta \in \mathbb{R}^p$ is drawn from a probability distribution P with mean μ_θ and covariance matrix Σ_θ . Conditional on θ , the coordinates of $Y = (Y(1), \dots, Y(p))^\top$ are drawn independently from a canonical one-parameter exponential family $Y(j) \sim p_{\theta(j)}(y)$, with density

$$p_{\theta(j)}(y) = \exp[\theta(j)y - A(\theta(j))] \quad (1)$$

$$Y(j)|\theta(j) \sim p_{\theta(j)}(y), \quad Y = (Y(1), \dots, Y(p))^\top. \quad (2)$$

The mean and variance of the random variable $Y(j)$ is $A'(\theta(j))$ and $A''(\theta(j))$. Therefore, the mean of Y conditional on θ is

$$X := \mathbb{E}(Y|\theta) = (A'(\theta(1)), \dots, A'(\theta(p)))^\top = A'(\theta),$$

so the noisy data vector Y can be expressed as $Y = A'(\theta) + \tilde{\varepsilon}$, with $\mathbb{E}(\tilde{\varepsilon}|\theta) = 0$ and the marginal mean of Y is $\mathbb{E}Y = \mathbb{E}A'(\theta)$. Thus, one can think of Y as a noisy realization of the clean vector $X = A'(\theta)$. However, the latent vector θ is also random and varies from sample to sample. In the XFEL application, $X = A'(\theta)$ are the unobserved noiseless images, and their randomness stems from the random (and unobserved) orientation of the molecule. We may write $Y = A'(\theta) + \text{diag}[A''(\theta)]^{1/2}\varepsilon$, where the coordinates of ε are conditionally independent and standardized given θ . The covariance of Y is given by the law of total covariance:

$$\begin{aligned} \text{Cov}[Y] &= \text{Cov}[\mathbb{E}(Y|\theta)] + \mathbb{E}[\text{Cov}[Y|\theta]] \\ &= \text{Cov}[A'(\theta)] + \mathbb{E} \text{diag}[A''(\theta)]. \end{aligned} \quad (3)$$

For the special case of Poisson observations $Y \sim \text{Poisson}_p(X)$, where $X \in \mathbb{R}^p$ is random, we can write $Y = X + \text{diag}(X)^{1/2}\varepsilon$. The natural parameter is the vector θ with $\theta(j) = \log X(j)$ and $A'(\theta(j)) = A''(\theta(j)) = \exp(\theta(j)) = X(j)$. Therefore, we have $\mathbb{E}Y = \mathbb{E}X$, and $\text{Cov}[Y] = \text{Cov}[X] + \mathbb{E} \text{diag}[X]$. In words, while the mean of the noisy images agrees with the mean of the clean images, their covariance matrices differ by a diagonal matrix that depends solely on the mean image.

Algorithm 1: Steerable e PCA and denoising

Input: Image data Y that contains n images of size $L \times L$

Output: Rotational invariant covariance estimator of noiseless images and denoised images

- 1 Compute the sample mean $\bar{Y} = \frac{1}{n} \sum_{i=1}^n Y_i$
 - 2 Estimate the support size R and band limit c from the mean image
 - 3 Compute the Fourier-Bessel expansion coefficients of $F(\bar{Y})$ and estimate the rotationally invariant sample mean \bar{f} as in Eq. (10)
 - 4 Compute the variance estimate $D_n = \text{diag}[\bar{f}]$
 - 5 Prewhiten (homogenize) the image data $Z = D_n^{-1/2}Y$
 - 6 Compute the truncated Fourier-Bessel expansion coefficients of $F(Z)$ and form the coefficients matrices $A^{(k)}$, for $k = 0, \dots, k_{\max}$
 - 7 **for** $k = 0, 1, \dots, k_{\max}$ **do**
 - 8 Compute the homogenized sample covariance matrix $S_{h,\gamma_k}^{(k)}$ as in Eq. (11) and its eigendecomposition $S_{h,\gamma_k}^{(k)} = \hat{W}\Lambda\hat{W}^*$
 - 9 Shrink the eigenvalues $S_{h,\gamma_k}^{(k)} = \hat{W}\eta_{\gamma_k}(\Lambda)\hat{W}^*$ of top r_k eigenvalues according to Eq. (14)
 - 10 Compute the recoloring matrix $B^{(k)}$ in eq. (18) and $D^{(k)}$ in eq. (20)
 - 11 Heterogenize the covariance matrix $S_{he}^{(k)} = (B^{(k)})^* \cdot S_{h,\gamma_k}^{(k)} \cdot B^{(k)}$
 - 12 Compute the scaling coefficients $\hat{\alpha}$ in Eq. (21) and keep components with $\hat{\alpha} > 0$
 - 13 Scale the covariance matrix $S_s^{(k)} = \sum \hat{\alpha}_i^{(k)} \hat{v}_i^{(k)} \left(\hat{v}_i^{(k)} \right)^*$, where the eigendecomposition of $S_{he}^{(k)}$ is $\sum \hat{v}_i^{(k)} \left(\hat{v}_i^{(k)} \right)^*$
 - 14 Denoise $\{A^{(k)}\}_{k=0}^{k_{\max}}$ as in Eqs. (23) and (24)
 - 15 **end**
 - 16 The rotational invariant covariance matrix estimator $\hat{S}((x, y), (x', y')) = G^{(0)}(x, y) S_s^{(0)} G^{(0)}(x', y')^* + 2 \sum_{k=1}^{k_{\max}} G^{(k)}(x, y) S_s^{(k)} G^{(k)}(x', y')^*$
 - 17 Reconstruct the denoised image using Eq. (25)
-

B. Fourier-Bessel Expansion

Under the observation model in Sec II-A, we develop a method that estimates the rotational invariant $\text{Cov}[X]$ efficiently and accurately from the image dataset Y . We assume that a digital image I is composed of discrete samples from a continuous function f with bandlimit c . The Fourier transform of f , denoted $\mathcal{F}(f)$, can be expanded in any orthogonal basis for the class of squared-integrable functions in a disk of radius c . For the purpose of steerable PCA, it is beneficial to choose a basis whose elements are products of radial functions with Fourier angular modes, such as the Fourier-Bessel functions. The scaled Fourier-Bessel functions are given by

$$\psi_c^{k,q}(\xi, \theta) = \begin{cases} N_{k,q} J_k \left(R_{k,q} \frac{\xi}{c} \right) e^{ik\theta}, & \xi \leq c, \\ 0, & \xi > c, \end{cases} \quad (4)$$

where (ξ, θ) are polar coordinates in the Fourier domain (i.e., $\xi_1 = \xi \cos \theta$, $\xi_2 = \xi \sin \theta$, $\xi \geq 0$, and $\theta \in [0, 2\pi)$; $N_{k,q} = (c\sqrt{\pi}|J_{k+1}(R_{k,q})|)^{-1}$ is the normalization factor; J_k is the Bessel function of the first kind of integer order k ; and $R_{k,q}$ is the q th root of the Bessel function J_k . We also assume that the functions of interest are concentrated in a disk of radius R in real domain. In order to avoid aliasing, we only use Fourier-Bessel functions that satisfy the following criterion [3], [25]

$$R_{k,q+1} \leq 2\pi cR. \quad (5)$$

For each angular frequency k , we denote by p_k the number of components satisfying Eq. (5). The total number of components is $p = \sum_{k=-k_{\max}}^{k_{\max}} p_k$, where k_{\max} is the maximal possible value of k satisfying Eq. (5). We also denote $\gamma_k = \frac{p_k}{2n}$ for $k > 0$ and $\gamma_0 = \frac{p_0}{n}$.

The inverse Fourier transform (IFT) of $\psi_c^{k,q}$ is

$$\begin{aligned} \mathcal{F}^{-1}(\psi_c^{k,q})(r, \phi) &= \frac{2c\sqrt{\pi}(-1)^q R_{k,q} J_k(2\pi cr)}{i^k (2\pi cr)^2 - R_{k,q}^2} e^{ik\phi} \\ &\equiv g_c^{k,q}(r) e^{ik\phi}, \end{aligned} \quad (6)$$

Therefore, we can approximate f using the truncated expansion

$$f(r, \phi) \approx \sum_{k=-k_{\max}}^{k_{\max}} \sum_{q=1}^{p_k} a_{k,q} g_c^{k,q}(r) e^{ik\phi}. \quad (7)$$

We evaluate the Fourier-Bessel expansion coefficients numerically as in [3] using a quadrature rule that consists of equally spaced points in the angular direction $\theta_l = \frac{2\pi l}{n_\theta}$, with $l = 0, \dots, n_\theta - 1$ and a Gaussian quadrature rule in the radial direction ξ_j for $j = 1, \dots, n_r$. To evaluate $a_{k,q}$, we need to sample the discrete Fourier transform of the image I , denoted $F(I)$, at the quadrature nodes,

$$\begin{aligned} F(I)(\xi_j, \theta_l) &= \frac{1}{2R} \sum_{i_1=-R}^{R-1} \sum_{i_2=-R}^{R-1} I(i_1, i_2) \\ &\quad \times \exp(-i2\pi(\xi_j \cos \theta_l i_1 + \xi_j \sin \theta_l i_2)), \end{aligned} \quad (8)$$

which can be evaluated efficiently using the the nonuniform discrete Fourier transform [26], and we get

$$a_{k,q} \approx \sum_{j=1}^{n_\xi} N_{k,q} J_{k,q} \left(\frac{\xi_j}{c} \right) \widehat{F(I)}(\xi_j, k) \xi_j w(\xi_j), \quad (9)$$

where $\widehat{F(I)}(\xi_j, k)$ is the 1D FFT of $F(I)$ on each concentric circle of radius ξ_j . For real-valued images, it is sufficient to evaluate the coefficients with $k \geq 0$, since $a_{-k,q} = a_{k,q}^*$. In addition, the coefficients have the following properties: under counter-clockwise rotation by an angle β , $a_{k,q}$ changes to $a_{k,q} e^{-ik\beta}$; and under reflection, $a_{k,q}$ changes to $a_{-k,q}$.

C. Prewhitening

Suppose I_1, \dots, I_n are n discretized input images sampled from f_1, \dots, f_n . Here, the observational vectors Y_i for ePCA are simply $Y_i = I_i$. In ePCA, the first step is to prewhiten the data using the sample mean. However, the sample mean $\bar{Y} = \frac{1}{n} \sum_{i=1}^n Y_i$ is not necessarily rotationally invariant. The

rotationally invariant sample mean can be evaluated from $\bar{a}_{k,q}$, the expansion coefficients of $F(\bar{Y})$,

$$\bar{f}(r, \phi) = \frac{1}{2\pi} \int_0^{2\pi} \frac{1}{n} \sum_{i=1}^n f_i(r, \phi - \alpha) d\alpha \approx \sum_{q=1}^{p_0} \bar{a}_{0,q} g_c^{0,q}(r). \quad (10)$$

The rotationally invariant sample mean is circularly symmetric. We denote by \bar{A} a vector that contains all the coefficients $\bar{a}_{0,q}$ ordered by the radial index q . Although the input images are non-negative, the finite truncation may result in small negative values in the mean estimation, so we threshold any negative entries to zero.

We prewhiten the images by the estimated mean image to create new images Z_1, \dots, Z_n as $Z_i(x, y) = \bar{f}(x, y)^{-1/2} Y_i(x, y)$, when $\bar{f}(x, y) > 0$, and $Z_i(x, y)$ is 0 otherwise. Combining Eqs. (5) and (9), we compute the truncated Fourier-Bessel expansion coefficients $a_{k,q}^i$ of $F(Z_i)$. Let us denote by $A^{(k)}$ the matrix of expansion coefficients with angular frequency k , obtained by putting $a_{k,q}^i$ into a matrix, where the columns are indexed by the image number i and the rows are ordered by the radial index q . The coefficient matrix $A^{(k)}$ is of size $p_k \times n$.

Since the truncated Fourier-Bessel transform is almost unitary [3], the rotationally invariant covariance kernel $\mathcal{S}((x, y), (x', y'))$ built from the original image data with all possible in-plane rotations and reflections can be computed in terms of the IFT of the Fourier-Bessel basis and the associated expansion coefficients. Subtracting the sample mean is equivalent to subtracting $\frac{1}{n} \sum_{j=1}^n a_{0,q}^j$ from the coefficients $a_{0,q}^i$, while keeping other coefficients unchanged. Therefore, we first update the zero angular frequency coefficients by $a_{0,q}^i \leftarrow a_{0,q}^i - \frac{1}{n} \sum_{j=1}^n a_{0,q}^j$. In terms of the expansion coefficients, the rotational invariant homogenized sample covariance matrix is $S_h = \bigoplus_{k=-k_{\max}}^{k_{\max}} S_h^{(k)}$, with

$$S_h^{(k)} = \frac{1}{n} \text{Re} \left\{ A^{(k)} \left(A^{(k)} \right)^* \right\}. \quad (11)$$

Let $\lambda_i^{(k)}$ and $\hat{w}_i^{(k)}$ be the eigenvalues and eigenvectors of $S_h^{(k)}$, respectively, that is

$$S_h^{(k)} = \sum_{i=1}^{p_k} \lambda_i^{(k)} \hat{w}_i^{(k)} (\hat{w}_i^{(k)})^* \quad (12)$$

D. Eigenvalue Shrinkage

For data with independent coordinates and equal variances, previous works [27]–[30] show that if the population spike ℓ is above the Baik-Ben Arous-Péché (BBP) phase transition, then the top sample spike pops out from the Marčenko-Pastur distribution of the “noise” eigenvalues. The top eigenvalue will converge to the value given by the *spike forward map*:

$$\lambda(\ell; \gamma_k) = \begin{cases} (1 + \ell) \left(1 + \frac{\gamma_k}{\ell} \right) & \text{if } \ell > \sqrt{\gamma_k}, \\ (1 + \sqrt{\gamma_k})^2 & \text{otherwise.} \end{cases} \quad (13)$$

The underlying clean population covariance eigenvalues can be estimated by solving the quadratic equation in Eq. (13). Shrinking the eigenvalues helps to denoise the block sample covariance matrices [31]. The shrinkers $\eta_{\gamma_k}(\lambda)$ set all noise

$$\hat{\ell} = \eta_{\gamma_k}(\lambda) = \begin{cases} (\lambda - 1 - \gamma_k + \sqrt{(\lambda - 1 - \gamma_k)^2 - 4\gamma_k})/2, & \lambda > (1 + \sqrt{\gamma_k})^2, \\ 0 & \lambda \leq (1 + \sqrt{\gamma_k})^2. \end{cases} \quad (14)$$

eigenvalues to zero for λ within the support of the Marčenko-Pastur distribution and reduce other eigenvalues according to Eq. (14). Then the denoised covariance matrices are

$$S_{h,\eta}^{(k)} = \sum_{i=1}^{r_k} \eta_{\gamma_k}(\lambda_i^{(k)}) \hat{w}_i^{(k)} (\hat{w}_i^{(k)})^*. \quad (15)$$

In the Gaussian standard spiked model the empirical and true eigenvectors have an asymptotically deterministic angle: $((w^{(k)})^* \hat{w}^{(k)})^2 \rightarrow c^2(\ell; \gamma_k)$ almost surely, where $c(\ell; \gamma_k)$ is the *cosine forward map* given by [29], [30]:

$$c^2(\ell; \gamma_k) = \begin{cases} \frac{1 - \gamma_k/\ell^2}{1 + \gamma_k/\ell} & \text{if } \ell > \sqrt{\gamma_k}, \\ 0 & \text{otherwise.} \end{cases} \quad (16)$$

We denote by \hat{c} an estimate of c using the estimated clean covariance eigenvalues $\hat{\ell}$ in Eq. (14) and $\hat{s}^2 = 1 - \hat{c}^2$.

E. Recoloring

Homogenization changes the direction of the clean eigenvectors. Therefore, after eigenvalue shrinkage, we recolor (heterogenize) the covariance matrix by conjugating the recoloring matrix B with $S_{h,\eta}$: $S_{he} = B^* \cdot S_{h,\eta} \cdot B$. The recoloring matrix is evaluated with numerical integration,

$$\begin{aligned} B_{k_1, q_1; k_2, q_2} &= \int_0^R \int_0^{2\pi} \sqrt{\tilde{f}(r)} \mathcal{F}^{-1}(\psi_c^{k_1, q_1})(r, \theta) \\ &\quad \times \left(\mathcal{F}^{-1}(\psi_c^{k_2, q_2})(r, \theta) \right) r dr d\theta \\ &= \int_0^R \sqrt{\tilde{f}(r)} g_c^{k_1, q_1}(r) \overline{g_c^{k_2, q_2}(r)} r dr \\ &\quad \times \int_0^{2\pi} e^{i(-k_1 + k_2)\theta} d\theta \\ &= \delta_{k_1, k_2} \int_0^R \sqrt{\tilde{f}(r)} g_c^{k_1, q_1}(r) \overline{g_c^{k_2, q_2}(r)} r dr, \end{aligned} \quad (17)$$

which has a block diagonal structure and is decoupled for each angular frequency, $B = \bigoplus_{k=-k_{\max}}^{k_{\max}} B^{(k)}$.

$$B_{q_1, q_2}^{(k)} = \int_0^R \sqrt{\tilde{f}(r)} g_c^{k, q_1}(r) \overline{g_c^{k, q_2}(r)} r dr. \quad (18)$$

Therefore, the recoloring step is also decoupled for each angular frequency sub-block. The heterogenized covariance estimators are

$$S_{he}^{(k)} = (B^{(k)})^* \cdot S_{h,\eta_{\gamma_k}}^{(k)} \cdot B^{(k)}. \quad (19)$$

Similar to Eq. (18), we define $D^{(k)}$ which will be used to scale the heterogenized covariance matrix estimator (see Eq. (21)) and denoise the expansion coefficients (see Eqs. (23) and (24)),

$$D_{q_1, q_2}^{(k)} = \int_0^R \tilde{f}(r) g_c^{k, q_1}(r) \overline{g_c^{k, q_2}(r)} r dr \quad (20)$$

F. Scaling

The eigendecomposition of $S_{he}^{(k)}$ gives $S_{he}^{(k)} = \sum_{i=1}^{r_k} \hat{v}_i^{(k)} (\hat{v}_i^{(k)})^*$. The empirical eigenvalues are $\hat{t} = \|\hat{v}^{(k)}\|^2$ which is a biased estimate of the true eigenvalue t . In [1, Sec. 4.2.3], a scaling rule was proposed to correct the bias. We extend it to the steerable case and scale each eigenvalue of $S_{he}^{(k)}$ by a parameter $\hat{\alpha}^{(k)}$,

$$\hat{\alpha}^{(k)} = \begin{cases} \frac{1 - \hat{s}^2 \tau^{(k)}}{\hat{c}^2}, & \text{for } 1 - \hat{s}^2 \tau^{(k)} > 0 \text{ and } \hat{c}^2 > 0 \\ 0 & \text{otherwise} \end{cases} \quad (21)$$

where the parameter $\tau^{(k)} = \frac{\text{tr} D^{(k)}}{p_k} \cdot \frac{\hat{\ell}}{\|\hat{v}^{(k)}\|^2}$. The scaled covariance matrices are

$$S_s^{(k)} = \sum_{i=1}^{r_k} \hat{\alpha}_i^{(k)} \hat{v}_i^{(k)} (\hat{v}_i^{(k)})^*. \quad (22)$$

The rotational invariant covariance kernel $\mathcal{S}((x, y), (x', y'))$ is well approximated by $\sum_{k=-k_{\max}}^{k_{\max}} G^{(k)}(x, y) S_s^{(k)} (G^{(k)}(x', y'))^*$, where $G^{(k)}$ contains IFT of all $\psi_c^{k, q}$ with angular frequency k . The computational complexity of steerable ePCA is $O(nL^3 + L^4)$, same as steerable PCA, and it is lower than the complexity of ePCA which is $O(\min(nL^4 + L^6, n^2L^2 + n^3))$.

G. Denoising

As an application of steerable ePCA, we develop a method to denoise the photon-limited images. Since the Fourier-Bessel expansion coefficients are computed from the prewhitened images, we first recolor the coefficients by multiplying $B^{(k)}$ with $A^{(k)}$ and then we apply Wiener-type filtering to denoise the coefficients. For the steerable basis expansion coefficients $A^{(k)}$ with angular frequency $k \neq 0$

$$\hat{A}^{(k)} = S_s^{(k)} (D^{(k)} + S_s^{(k)})^{-1} B^{(k)} A^{(k)} \quad (23)$$

For $k = 0$, we need to take into account the rotational invariant mean expansion coefficients,

$$\begin{aligned} \hat{A}^{(0)} &= S_s^{(0)} (D^{(0)} + S_s^{(0)})^{-1} B^{(0)} A^{(0)} \\ &\quad + D^{(0)} (D^{(0)} + S_s^{(0)})^{-1} \bar{A} \mathbf{1}_n^\top. \end{aligned} \quad (24)$$

The denoised image sampled on the Cartesian grid (x, y) in real domain are computed from the filtered expansion coefficients $\hat{a}_{k, q}^i$,

$$\begin{aligned} \hat{X}_i(x, y) &= \sum_{q=1}^{p_0} \hat{a}_{0, q}^i g_c^{0, q}(r_{x, y}) \\ &\quad + 2\text{Re} \left[\sum_{k=1}^{k_{\max}} \sum_{q=1}^{p_k} \hat{a}_{k, q}^i g_c^{k, q}(r_{x, y}) e^{-ik\theta_{x, y}} \right], \end{aligned} \quad (25)$$

where $r_{x, y} = \sqrt{x^2 + y^2}$ and $\theta_{x, y} = \tan^{-1}(\frac{y}{x})$.

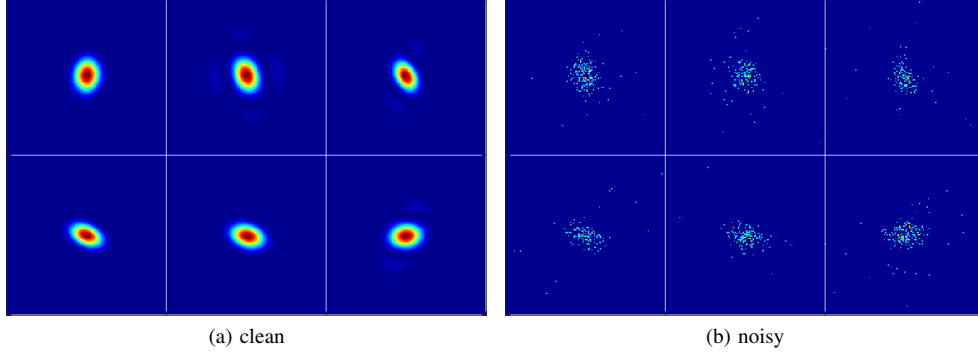


Fig. 1: Sample clean and noisy images of the XFEL dataset. Image size is 128×128 with mean photon count=0.1.

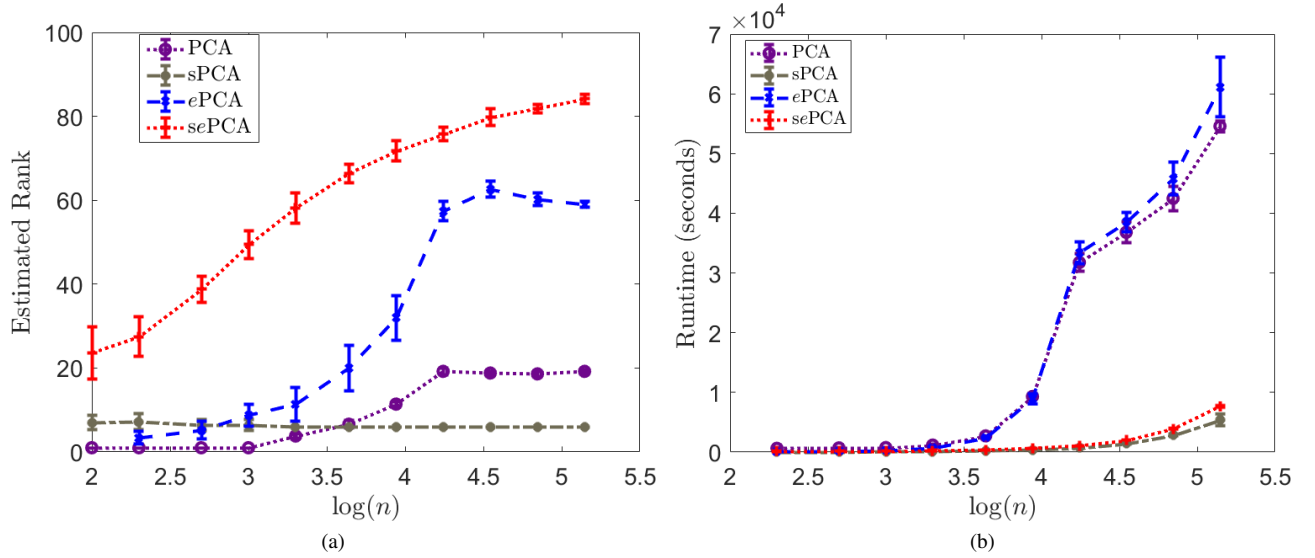


Fig. 2: (a) The estimated number of signal principal components using PCA, steerable PCA (sPCA), e PCA and steerable e PCA (sePCA) and (b) the corresponding runtimes for computing the principal components. The sample size n ranges from 100 to 140,000. Images are corrupted by Poisson noise with mean photon count 0.01.

III. NUMERICAL RESULTS

We apply steerable e PCA and e PCA to a simulated XFEL dataset and compare the results for covariance estimation and denoising. The algorithms are implemented in MATLAB on a machine with 60 cores, running at 2.3 GHz, with total RAM of 1.5TB. For steerable e PCA and steerable PCA, but only 8 cores were used in our experiments. We simulate $n = 140000$ noiseless XFEL diffraction intensity maps of a lysozyme (Protein Data Bank 1AKI) with Condor [32]. The average pixel intensity is rescaled to be 0.01 for image size 128×128 pixels such that shot noise dominates [33]. To sample an arbitrary number n of noisy diffraction patterns, we sample an intensity map at random, in-plane rotate the sample by a random angle following a uniform distribution over $[0, 2\pi)$, and then sample the photon count of each detector pixel from a Poisson distribution whose mean is the pixel intensity. Figures 1a and 1b illustrate the clean intensity maps and the resulting noisy diffraction patterns.

A. Covariance estimation and principal components

For experiments using e PCA, we use a permutation bootstrap-based method to estimate the rank of the covariance matrix, following e.g. [34]. By randomly permuting each column of the mean-subtracted data matrix, we completely destroy structural information including linear structure, while the noise statistics remain the same (see [35], [36] for an analysis). Singular values of the randomly permuted matrices reveal what should be the largest covariance matrix eigenvalues that correspond to noise, up to a user-selected confidence level β . This can replace the other rank estimation methods that assume Gaussian distribution when the noise model is non-Gaussian, such as in our case. Empirically, we observe that $\beta = 0.1$ gives the best performance in covariance estimation. For steerable e PCA, we estimate the number of components using the right edge of the Marčenko-Pastur distribution for homogenized covariance matrices $S_h^{(k)}$ and include only the components whose scaling factor $\hat{\alpha}^{(k)}$ are above zero.

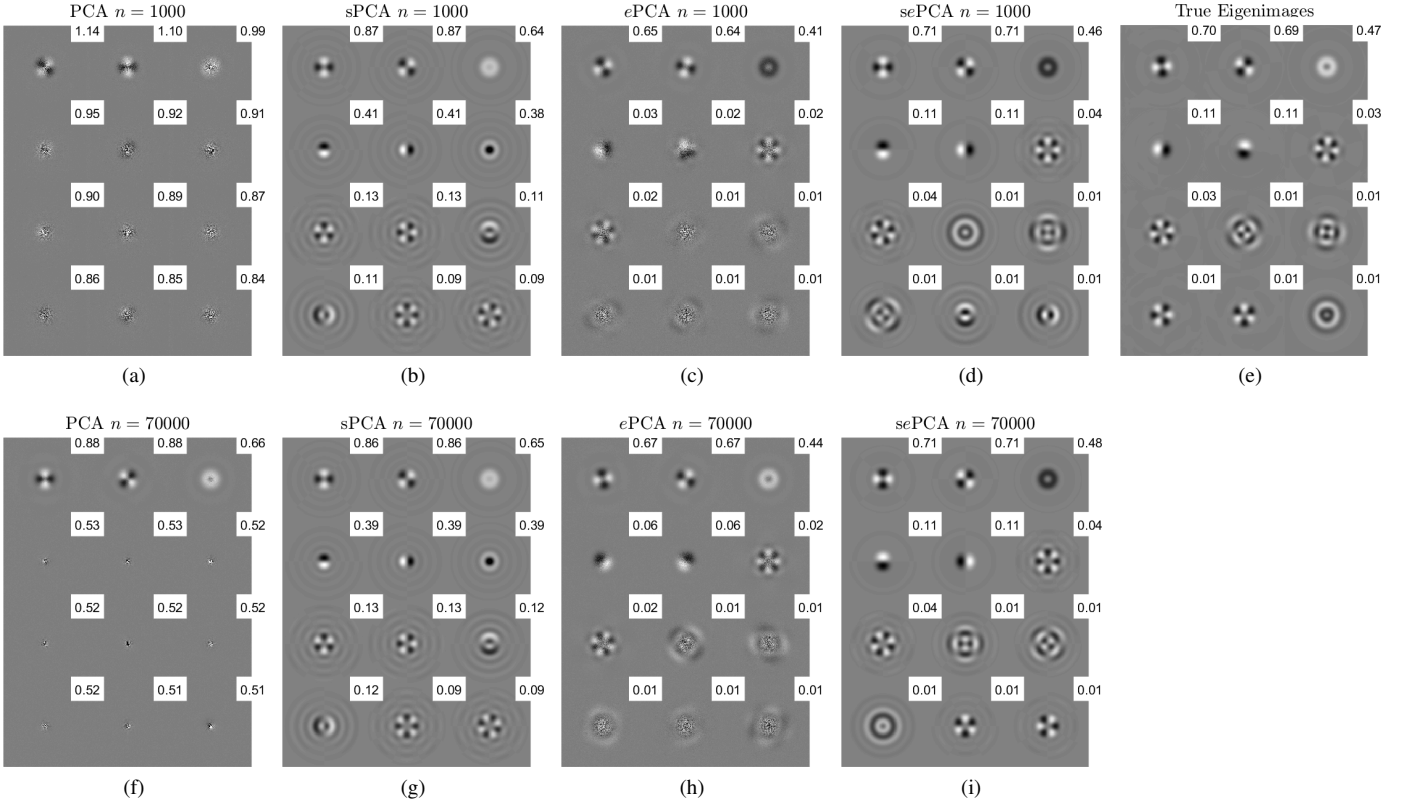


Fig. 3: Eigenimages estimated from noisy XFEL data using PCA, sPCA, ePCA, sePCA, ordered by eigenvalues. Input images are corrupted by Poisson noise with mean photon count 0.01 (shown in Figure 1b).

Steerable ePCA is able to recover more signal principal components from noisy images than PCA, steerable PCA, and ePCA (see Fig. 2a). When the sample size $n = 1000$, the mean number of estimated components is 11 and 49 for ePCA and steerable ePCA respectively. For $n = 70000$, the estimated number of components is 59 and 81 for ePCA and steerable ePCA respectively. Fig. 2b shows that steerable ePCA is more efficient than ePCA and PCA. Because steerable ePCA contains extra steps such as prewhitening, recoloring, and scaling, its runtime is slightly larger than steerable PCA. When $n = 140000$, steerable ePCA is 8 times faster than ePCA.

Fig. 3 shows the top 12 eigenimages for clean XFEL diffraction patterns (Fig. 3e), and noisy diffraction patterns with mean photon count 0.01 (Figs. 3c–3i) using PCA, steerable PCA, ePCA, and steerable ePCA. The true eigenimages in Fig. 3e are computed from 70000 clean diffraction patterns whose orientations are uniformly distributed over $SO(3)$. Figs. 3a–3d are computed from 1000 noisy images. Since the number of samples is much smaller than the size of the image and the noise type is non-Gaussian, PCA can only recover the first two or three components. ePCA improves the estimation and is able to extract the top 7 eigenimages. Moreover, steerable PCA and steerable ePCA achieve much better estimation of the underlying true eigenimages for a given sample size. Steerable ePCA achieves the best performance in estimating both the eigenvalues and eigenimages.

Furthermore, we compare the operator norms and Frobenius norms of the difference between the covariance estimates and the true covariance matrix. Fig. 4 shows that steerable ePCA

significantly improves the covariance estimation, especially when the sample size is small.

B. Denoising

We compare the denoising effects of ePCA and steerable ePCA by the mean squared error, $MSE := (pn)^{-1} \sum_{i=1}^n \|\hat{X}_i - X_i\|^2$. We perform “ePCA denoising” using empirical best linear predictor (EBLP) [1], which had been shown to outperform “PCA denoising”, i.e., orthogonal projection onto sample or ePCA/heterogenized eigenimages, as well as the exponential family PCA method proposed by [37]. Note that in our implementation, to avoid inverting a singular matrix (when some coordinates have 0 sample mean and sample variance), we compute $\text{diag}[\bar{Y}] + S_s$ with ‘regularization’, $\text{diag}[\bar{Y}] + S_s \leftarrow S_s + (1 - \epsilon) * \text{diag}[\bar{Y}] + \epsilon * m * I$ where $\epsilon = 0.1$, $m = \frac{1}{p} \bar{Y} \cdot \mathbf{1}$, and I is the p by p identity matrix. The number of components are estimated by the permutation rank estimation as described in the previous section.

Steerable ePCA is able to recover the images with lower MSEs compared to PCA, steerable PCA, and ePCA (see Fig. 6), especially when the sample size n is small. Fig. 5 shows some examples of denoised images for sample size $n = 1000$ and 70000. For robustness, we repeated the numerical experiment for another dataset simulated from the small protein chignolin (Protein Data Bank entry 1UAO) and obtained qualitatively similar results.

IV. CONCLUSION

We presented steerable ePCA, a method for principal component analysis of a set of low-photon count images and

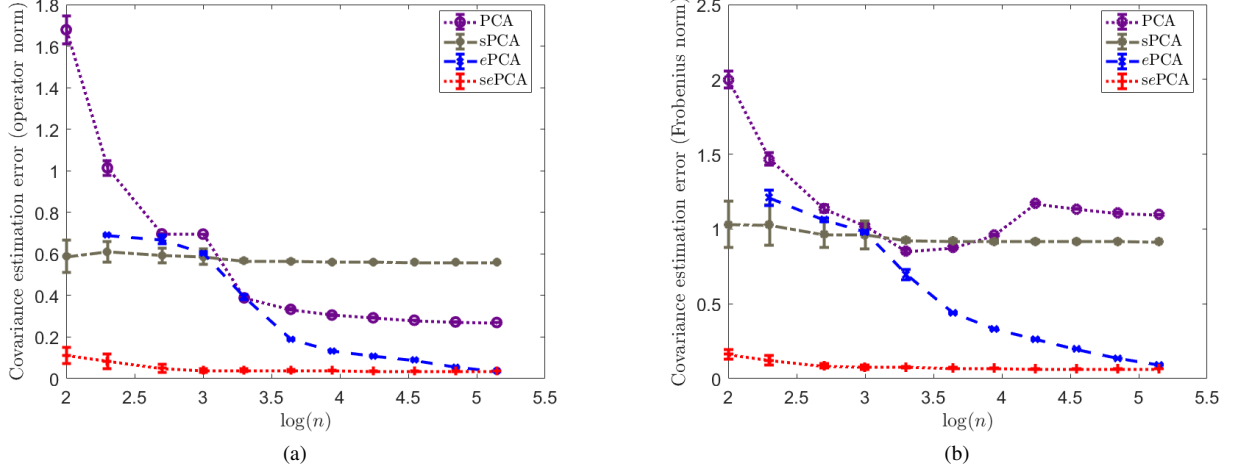


Fig. 4: Error of covariance matrix estimation, measured as the operator norm (left) and Frobenius norm (right) of the difference between each covariance estimate and the true covariance matrix.

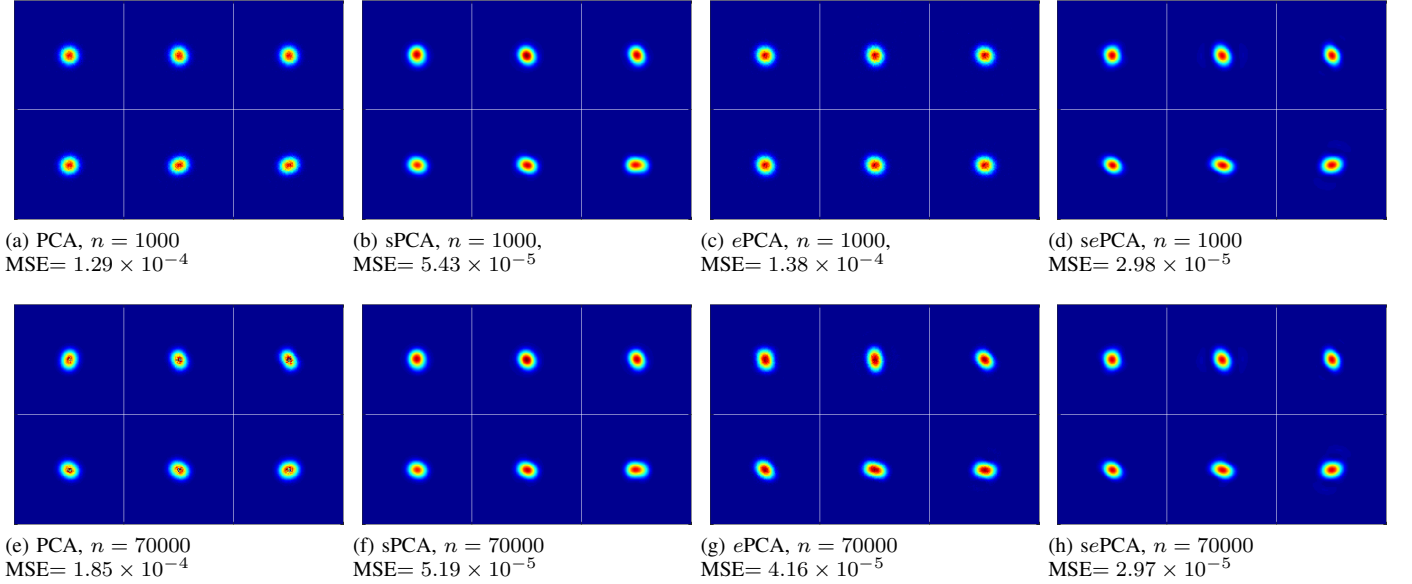


Fig. 5: Sample denoised images of the XFEL dataset illustrated in Fig. 1 using PCA, steerable PCA (sPCA), ePCA, and steerable ePCA (sePCA). Image size is 128×128 .

their uniform in-plane rotations. This work has been mostly motivated by its application to XFEL. The computational complexity of the new algorithm is $O(nL^3 + L^4)$, whereas that of ePCA is $O(\min(nL^4 + L^6, n^2L^2 + n^3))$. Incorporating rotational invariance allows more robust estimation of the true eigenvalues and eigenvectors. Our numerical experiments showed that steerable ePCA is able to recover more signal components than ePCA and achieves better covariance estimation and denoising results. Finally, we remark that the Fourier-Bessel basis can be replaced with other suitable bases, for example, the 2-D prolate spheroidal wave functions (PSWF) on a disk [38], [39].

ACKNOWLEDGMENTS

The authors would like to thank Edgar Dobriban and Boris Landa for discussions. ZZ is partially supported by National Center for Supercomputing Applications Faculty Fellowship and University of Illinois at Urbana-Champaign College of Engineering Strategic Research Initiative. AS is partially supported by Award Number R01GM090200 from the NIGMS, FA9550-17-1-0291 from AFOSR, Simons Investigator Award, the Moore Foundation Data-Driven Discovery Investigator Award, and NSF BIGDATA Award IIS-1837992.

REFERENCES

- [1] L. T. Liu, E. Dobriban, and A. Singer, “ePCA: High dimensional exponential family PCA,” *Annals of Applied Statistics*, vol. 12, no. 4,

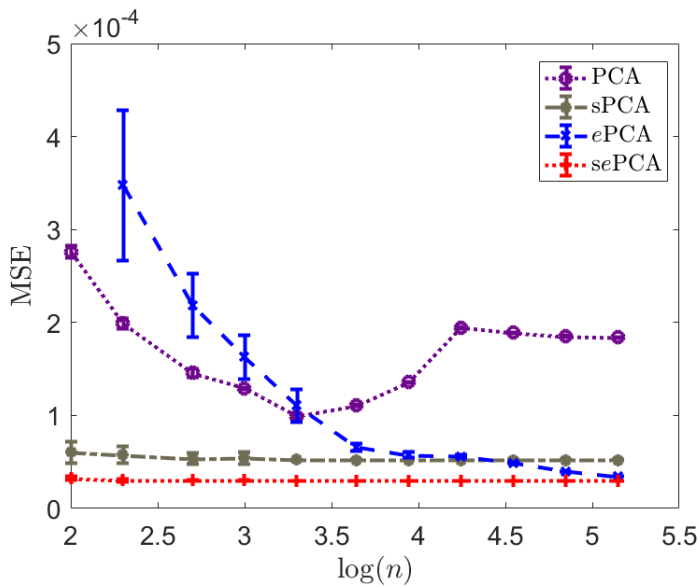


Fig. 6: Comparing sampled reconstructions of the XFEL dataset ($p = 16384$) with various number of images.

- pp. 2121–2150, 2018.
- [2] Z. Zhao and A. Singer, “Rotationally invariant image representation for viewing direction classification in cryo-em,” *Journal of Structural Biology*, vol. 186, no. 1, pp. 153–166, 2014.
 - [3] Z. Zhao, Y. Shkolnisky, and A. Singer, “Fast steerable principal component analysis,” *IEEE Transactions on Computational Imaging*, vol. 2, no. 1, pp. 1–12, 2016.
 - [4] V. Favre-Nicolin, J. Baruchel, H. Renevier, J. Eymery, and A. Borbély, “XTOP: high-resolution X-ray diffraction and imaging,” *Journal of Applied Crystallography*, vol. 48, no. 3, pp. 620–620, 2015.
 - [5] F. R. N. C. Maia and J. Hajdu, “The trickle before the torrent—X-ray diffraction data from X-ray lasers,” *Scientific Data*, vol. 3, 2016.
 - [6] S. H. W. Scheres, H. Gao, M. Valle, G. T. Herman, P. P. B. Eggermont, J. Frank, and J.-M. Carazo, “Disentangling conformational states of macromolecules in 3D-EM through likelihood optimization,” *Nature Methods*, vol. 4, no. 1, pp. 27–29, 2007.
 - [7] D. N.-T. Loh and V. Elser, “Reconstruction algorithm for single-particle diffraction imaging experiments,” *Phys. Rev. E*, vol. 80, p. 026705, Aug 2009.
 - [8] Z. Kam, “Determination of macromolecular structure in solution by spatial correlation of scattering fluctuations,” *Macromolecules*, vol. 10, no. 5, pp. 927–934, 1977.
 - [9] D. K. Saldin, V. L. Shneerson, R. Fung, and A. Ourmazd, “Structure of isolated biomolecules obtained from ultrashort X-ray pulses: exploiting the symmetry of random orientations,” *Journal of Physics: Condensed Matter*, vol. 21, no. 13, 2009.
 - [10] D. Starodub, A. Aquila, S. Bajt, M. Barthelmess, A. Barty, C. Bostedt, J. D. Bozek, N. Coppola, R. B. Doak, S. W. Epp *et al.*, “Single-particle structure determination by correlations of snapshot X-ray diffraction patterns,” *Nature communications*, vol. 3, p. 1276, 2012.
 - [11] K. Pande, P. Schwander, M. Schmidt, and D. K. Saldin, “Deducing fast electron density changes in randomly orientated uncrystallized biomolecules in a pump-probe experiment,” *Phil. Trans. R. Soc. B*, vol. 369, no. 1647, p. 20130332, 2014.
 - [12] R. P. Kurta, J. J. Donatelli, C. H. Yoon, P. Berntsen, J. Bielecki, B. J. Daurer, H. DeMirici, P. Fromme, M. F. Hantke *et al.*, “Correlations in scattered X-ray laser pulses reveal nanoscale structural features of viruses,” *Physical Review Letters*, vol. 119, no. 15, p. 158102, 2017.
 - [13] J. J. Donatelli, J. A. Sethian, and P. H. Zwart, “Reconstruction from limited single-particle diffraction data via simultaneous determination of state, orientation, intensity, and phase,” *Proceedings of the National Academy of Sciences*, vol. 114, no. 28, pp. 7222–7227, 2017.
 - [14] B. von Ardenne, M. Mechelke, and H. Grubmüller, “Structure determination from single molecule X-ray scattering with three photons per image,” *Nat Commun.*, vol. 9, no. 1, p. 2375, 2018.
 - [15] K. Pande, J. J. Donatelli, E. Malmerberg, L. Foucar, C. Bostedt, I. Schlichting, and P. H. Zwart, “Ab initio structure determination from experimental fluctuation x-ray scattering data,” *Proceedings of the National Academy of Sciences*, vol. 115, no. 46, pp. 11 772–11 777, 2018. [Online]. Available: <http://www.pnas.org/content/115/46/11772>
 - [16] I. Jolliffe, *Principal Component Analysis*. Wiley Online Library, 2002.
 - [17] T. W. Anderson, *An Introduction to Multivariate Statistical Analysis*. Wiley New York, 2003.
 - [18] R. D. Nowak and R. G. Baraniuk, “Wavelet-domain filtering for photon imaging systems,” *IEEE Transactions on Image Processing*, vol. 8, no. 5, pp. 666–678, 1999.
 - [19] F. Luisier, T. Blu, and M. Unser, “A new sure approach to image denoising: Interscale orthonormal wavelet thresholding,” *IEEE Transactions on image processing*, vol. 16, no. 3, pp. 593–606, 2007.
 - [20] F. J. Anscombe, “The transformation of poisson, binomial and negative-binomial data,” *Biometrika*, vol. 35, no. 3-4, p. 246, 1948.
 - [21] J.-L. Starck, F. Murtagh, and J. M. Fadili, *Sparse image and signal processing: wavelets, curvelets, morphological diversity*. Cambridge university press, 2010.
 - [22] T. Furnival, R. K. Leary, and P. A. Midgley, “Denoising time-resolved microscopy image sequences with singular value thresholding,” *Ultra-microscopy*, 2016.
 - [23] Y. Cao and Y. Xie, “Low-rank matrix recovery in Poisson noise,” in *Signal and Information Processing (GlobalSIP), 2014 IEEE Global Conference on*. IEEE, 2014, pp. 384–388.
 - [24] M. Sonnleitner, J. Jeffers, and S. M. Barnett, “Local retrodiction models for photon-noise-limited images,” in *SPIE Photonics Europe*. International Society for Optics and Photonics, 2016, pp. 98 960V–98 960V.
 - [25] A. Klug and R. A. Crowther, “Three-dimensional image reconstruction from the viewpoint of information theory,” *Nature*, vol. 238, pp. 435–440, 1972.
 - [26] L. Greengard and J. Lee, “Accelerating the Nonuniform Fast Fourier Transform,” *SIAM Review*, vol. 46, no. 3, pp. 443–454, 2004.
 - [27] J. Baik, G. Ben Arous, and S. Péché, “Phase transition of the largest eigenvalue for nonnull complex sample covariance matrices,” *Annals of Probability*, vol. 33, no. 5, pp. 1643–1697, 2005.
 - [28] J. Baik and J. W. Silverstein, “Eigenvalues of large sample covariance matrices of spiked population models,” *Journal of Multivariate Analysis*, vol. 97, no. 6, pp. 1382–1408, 2006.
 - [29] D. Paul, “Asymptotics of sample eigenstructure for a large dimensional spiked covariance model,” *Statistica Sinica*, vol. 17, no. 4, pp. 1617–1642, 2007.
 - [30] F. Benaych-Georges and R. R. Nadakuditi, “The eigenvalues and eigenvectors of finite, low rank perturbations of large random matrices,” *Advances in Mathematics*, vol. 227, no. 1, pp. 494–521, 2011.
 - [31] D. L. Donoho, M. Gavish, and I. M. Johnstone, “Optimal shrinkage of eigenvalues in the Spiked Covariance Model,” *Annals of Statistics*, vol. 46, no. 4, p. 1742, 2018.
 - [32] M. F. Hantke, T. Ekeberg, and F. R. N. C. Maia, “Condor: A simulation tool for flash X-ray imaging,” *Journal of Applied Crystallography*, vol. 49, no. 4, p. 1356a–1362, 2016.
 - [33] P. Schwander, D. Giannakis, C. H. Yoon, and A. Ourmazd, “The symmetries of image formation by scattering. II. Applications,” *Opt. Express*, vol. 20, no. 12, pp. 12 827–12 849, Jun 2012.
 - [34] J. Landgrebe, W. Wurst, and G. Welzl, “Permutation-validated principal components analysis of microarray data,” *Genome Biology*, vol. 3, no. 4, 2002.
 - [35] E. Dobriban, “Permutation methods for factor analysis and PCA,” *arXiv preprint arXiv:1710.00479*, Oct. 2017.
 - [36] E. Dobriban and A. B. Owen, “Deterministic parallel analysis: an improved method for selecting factors and principal components,” *Journal of the Royal Statistical Society: Series B (Statistical Methodology)*, 2018.
 - [37] M. Collins, S. Dasgupta, and R. E. Schapire, “A generalization of principal component analysis to the exponential family,” *Advances in Neural Information Processing Systems (NIPS)*, 2001.
 - [38] D. Slepian, “Prolate spheroidal wave functions, Fourier analysis, and uncertainty—IV: extensions to many dimensions, generalized prolate spheroidal wave functions,” *Bell System Technical Journal*, vol. 43, pp. 3009–3057, 1964.
 - [39] B. Landa and Y. Shkolnisky, “Steerable principal components for space-frequency localized images,” *SIAM Journal on Imaging Sciences*, vol. 10, no. 2, pp. 508–534, 2017.